Physics-Informed Token Prediction-Based Dynamic Modeling and High-Speed Feedforward Tracking Control of Dielectric Elastomer Actuators

Xingyu Chen, *Student Member, IEEE*, Xiaotian Shi, Peinan Yan, *Student Member, IEEE*, Jieji Ren, Guoying Gu, *Senior Member, IEEE*, and Jiang Zou, *Member, IEEE*

***Abstract*—Due to their continuous electromechanical deformation, rate-dependent viscoelasticity, and complex mechanical vibration, dynamic modeling and high-speed tracking control of dielectric elastomer actuators (DEAs) remain elusive, significantly limiting their working bandwidth. In this work, we propose a physics-informed token prediction (PITP) that enables accurate modeling of DEA dynamics and high-speed feedforward tracking control. The PITP framework consists of two key components: a physics-informed encoder and a dynamic decoder. The physics-informed encoder is designed based on a simplified equivalent linear model and trained through the hierarchical optimization training method, which embeds the global dynamic characteristics into tokens, minimizing the need for extensive data and training. Then, the dynamic decoder is developed by using these tokens as state-dependent parameters, capable of describing complex dynamic responses through the autoregressive solution. Finally, by taking advantage of the model's reversibility, a direct inverse compensator is established to linearize the input–output relationship. Experimental results of several DEAs with different configurations and payloads demonstrate that, based on our PITP framework, the complex nonlinear dynamic responses of all DEAs can be precisely described and eliminated within their natural frequency, validating its generality and versatility. By leveraging fast modeling (<30 min) and high-speed feedforward tracking control, our PITP framework may accelerate DEAs' practical applications.**

***Index Terms*—Dielectric elastomer actuators (DEAs), dynamic modeling, high-precision tracking control, physics-informed token prediction (PITP).**

Received 20 September 2025; revised 2 December 2025; accepted 19 December 2025. Date of publication 14 January 2026; date of current version 27 January 2026. This work was supported in part by the National Key R&D Program of China under Grant 2024YFB4707504, in part by the National Natural Science Foundation of China under Grant 52275024, in part by the Natural Science Foundation of Shanghai under Grant 23ZR1435500 and Grant 24511103400, and in part by the Chenguang Program of Shanghai Education Development Foundation and Shanghai Municipal Education Commission. This article was recommended for publication by Associate Editor Y. Liu and Editor H. Zhao upon evaluation of the reviewers' comments. *(Corresponding author: Jiang Zou.)*

The authors are with the State Key Laboratory of Mechanical System and Vibration, School of Mechanical Engineering, Shanghai Jiao Tong University, Shanghai 200240, China, and also with the Shanghai Key Laboratory of Intelligent Robotics, Shanghai Jiao Tong University, Shanghai 200240, China (e-mail: afterglow777@sjtu.edu.cn; sjtu_sxt@sjtu.edu.cn; peinanyan@sjtu.edu.cn; jiejiren@sjtu.edu.cn; guguoying@sjtu.edu.cn; zoujiang@sjtu.edu.cn).

Digital Object Identifier 10.1109/TRO.2026.3653783

I. Introduction

DIELECTRIC elastomer actuators (DEAs) have garnered significant attention in the field of soft robotics owing to their fast response speed, high energy density, and large deformation [1], [2]. DEAs typically consist of a sandwich-structured dielectric film and a fixed frame [3]. When a high voltage is applied across the thin elastomeric film sandwiched between two compliant electrodes, the film is compressed, leading to an increase in area and a decrease in thickness due to Maxwell stress [see Fig. 1(a)]. Based on this working principle, DEAs with various configurations have been designed to achieve different types of motion, such as planar DEAs [4], conical DEAs [5], minimum energy structure DEAs [6], rolled DEAs [7], and stacked DEAs [8], showing wide applications, such as climbing robots [9], flying robots [10], deep-sea robots [11], and wearable robotics [12]. As their emerging applications, dynamic modeling and precise control of DEAs are highly desired. However, it remains a significant challenge due to the complex dynamic characteristics of DEAs [see Fig. 1(b)], including rate-dependent viscoelasticity, mechanical resonance, and their coupling [13], [14]. Especially, some high power density DEAs [15], [16] exhibit high natural frequency (>100 Hz) and serious resonance, increasing the difficulty of modeling and control.

In previous work, a lot of attention has been paid to solving the above-mentioned problem. To date, existing approaches are mainly categorized into four categories: distributed-parameter approaches, phenomenological approaches, lumped-parameter based approaches, and learning-based approaches. In general, distributed-parameter approaches usually adopt continuum mechanics and nonequilibrium thermodynamics [17], [18] to develop distributed-parameter models for DEAs, capable of explaining their physic phenomena, such as electromechanical deformation and rate-dependent viscoelasticity. However, these models generally consist of several partial differential equations, which are difficult to be converted into the control model because of their complexity. Different from distributed-parameter approaches, some phenomenological approaches introduce mathematical models (e.g., the Preisach model [19] and the Prandtl–Ishlinskii model [20], [21]) to characterize the dynamic behavior of DEAs. Those models only rely on the experimental data without taking the physical insight into consideration, showing the advantage of fewer parameters and ease of use. In the

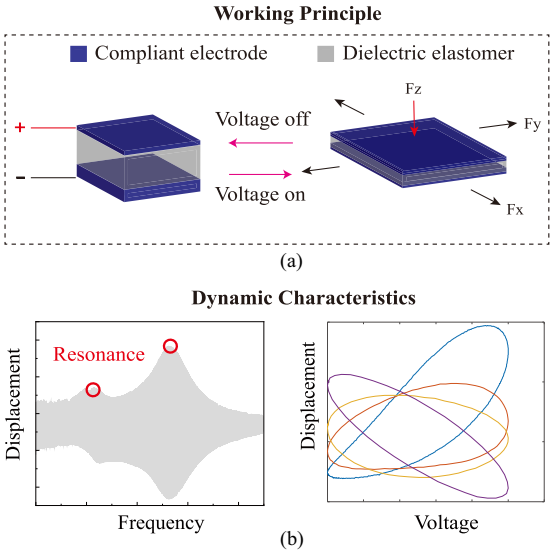

Fig. 1. (a) Working principle of DEAs. (b) Dynamic response of the sweep and the rate-dependent hysteresis circles.

meantime, those models can be used to design controllers, such as direct inverse hysteresis compensation [22], model predictive control [23], and model-based adaptive control [24]. Since phenomenological models are developed without considering physical properties, they fail to capture mechanical vibration phenomena, limiting their working bandwidth. To overcome the limitations of phenomenological models, lumped-parameter models [25], [26], [27] have been proposed. These models simplify the DEA into a lumped-parameter dynamic system, which can accurately describe the rate-dependent viscoelasticity, mechanical resonance, and their coupling. Then, several controllers can be developed, such as nonlinear PID [28], H-infinity [29], sliding mode control [30], and neural-implicit embedded controller [31]. Due to the presence of unmeasurable states in lumped parameter models, obtaining a direct inverse model is challenging. Consequently, existing control strategies often rely on observers and operate in a closed-loop framework, which necessitates the use of integrated rigid sensors and limits the application flexibility of soft actuators. Achieving direct inverse feedforward compensation for rate-dependent viscoelasticity and hysteresis remains a significant challenge. Owing to their remarkable ability to capture nonlinear relationships, machine learning techniques provide promising solutions for the dynamic modeling and control of DEAs. For example, gated recurrent unit (GRU) based inverse models [32], long short term memory (LSTM) based models [33], and the nonlinear autoregressive with exogenous inputs (NARX) based self-sensing models [34] have been developed based on large datasets and extensive training. Nevertheless, since these approaches are directly trained on experimental data, they are often highly dependent on data quality and quantity, and collecting sufficient high-quality data can be both time-consuming and costly. Consequently, their practical performance is usually constrained within relatively low-frequency ranges, which may limit their applicability in broader band control scenarios. Therefore, the dynamic modeling and control of DEAs remain elusive.

Inspired by the concept of "token," which is popularly used in language sequence generation [35], [36], we explore a new perspective for the dynamic modeling and control of DEAs. By encoding, predicting, and decoding tokens through machine learning approaches, the task of language understanding and generation is transformed into predicting the next token. Drawing on this idea, this work proposes a physics-informed token prediction (PITP)-based dynamic model and the feedforward control strategy for DEAs (see Fig. 2). At first, the dynamic state of DEAs is regarded as the smallest unit in a motion sequence, and the dynamic responses can be decomposed into the steps of encoding, predicting, and decoding this unit. To reduce the training time and the need for experimental data, we design and train a physics-informed encoder based on a simplified equivalent linear model. We further propose a training method to treat the physical boundaries as hyperparameters to optimize hierarchically, enhancing the nonlinear descriptive capability of the model. Then, the nonlinear dynamic model is developed by using the tokens as state-dependent parameters. It can precisely describe complex dynamic responses through the autoregressive solution. Finally, based on the proposed dynamic model, the direct inverse feedforward control is straightforwardly derived and applied to the feedforward control of DEAs. Experimental results demonstrate the versatility and effectiveness of the proposed model and its corresponding feedforward control strategy across different DEA configurations and payloads within a wide frequency range (exceeding 143 Hz).

The main contribution of this work can be concluded as follows.

1) A PITP-based dynamic modeling strategy is proposed, introducing the first tokenized dynamic model for DEAs. This approach addresses complex nonlinear dynamics and ensures reversibility by decomposing the dynamics into physics-informed encoding and decoding stages, achieving accurate representation with reduced data requirements and enabling high-speed feedforward control across diverse configurations and payloads.
2) Based on the PITP-based dynamic modeling strategy, the resultant models are invertible and can be used to construct feedforward controllers. Without the external sensors, it can reduce the complexity of controller design, contributing to improving the ease of use.

The rest of this article is organized as follows. Section II introduces the PITP for generalized dynamic modeling and the feedforward control strategy of DEAs. Section III presents the experimental results of the prediction of the dynamic model and the feedforward open-loop control. In Section IV, the ablation study and further discussion of the PITP are provided. Finally, Section V concludes this article.

II. Dynamic Modeling and Feedforward Control of DEAs Based on PITP

In general, to describe the dynamic responses of DEAs, it is essential to characterize the relationship between the excitation voltage u and the output displacement x of the end effector. Due to the dynamic features of DEAs, the displacement of DEA

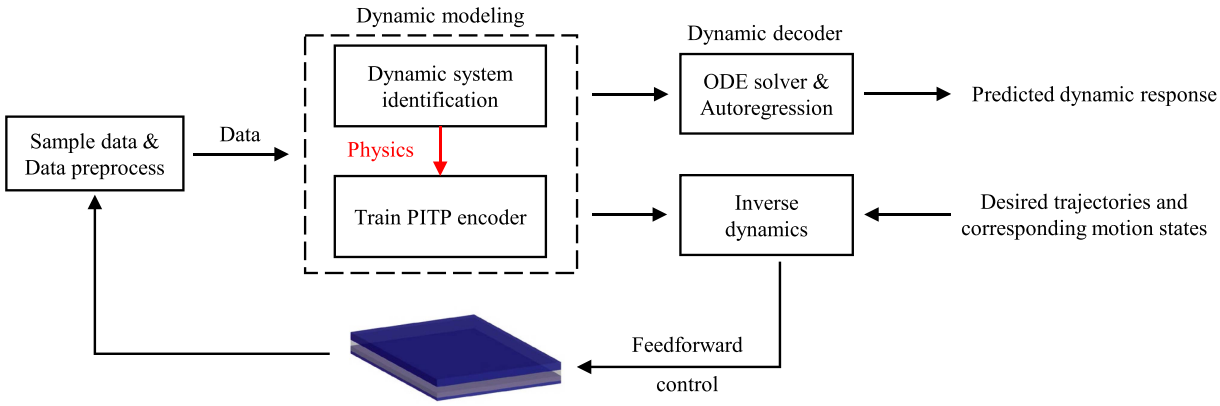

Fig. 2. Framework of general dynamic modeling and control of DEAs based on PITP.

x is typically influenced by nonlinear electromechanical coupling, mechanical vibration, and rate-dependent viscoelasticity. Therefore, the primary goal of dynamic modeling is to accurately characterize these features. Viscoelastic nonlinearities are considered a form of energy dissipation [13] and are typically described using rheological elements. However, these elements introduce additional unmeasurable state variables, making the model unsuitable for direct inversion in feedforward control. To address this issue, it is essential to ensure that all state variables in the dynamic model are measurable. Accordingly, the dynamic modeling problem is formulated in a discrete-time framework as follows, where the system's state is updated at each time step, and the dynamic behavior is described through discrete state transitions:

$$\begin{aligned} X_{t+1}^m &= g(X_t^m, u_t) \\ X_t^m &= \left[x_t^0, x_t^1, \ldots, x_t^m\right]^T \\ x_t^m &= \frac{d^m x_t}{dt^m} \end{aligned} \tag{1}$$

where $X_t^m \in \mathbb{R}^{m\times 1}$, $x_t \in \mathbb{R}$, and $u_t \in \mathbb{R}$ represent the m-dimensional motion state, output displacement, and external excitation of the DEA at timestamp t, respectively; g denotes the nonlinear function describing the discrete state transition. However, the complexity involved in designing g increases the difficulty of directly inverting the model for control purposes. Inspired by the concept of token prediction, we introduce physics-informed tokens to represent the nonlinear dynamic process. These physics-informed tokens implicitly embed the underlying dynamic generation mechanism: they can be encoded from the current motion state and, when combined with external excitations, decoded to predict the subsequent motion state. Then, the encoding process of the tokens is responsible for capturing nonlinearities, while the prediction and decoding are designed to remain simple and invertible. In this way, the complex nonlinearities are effectively captured while preserving the invertibility of the dynamic model. In this study, we employ a deep network to realize the nonlinear encoding process, whereas the prediction and decoding of the tokens are modeled using a simple linear dynamic system. As a consequence, the dynamic process is decomposed into the following stages:

$$\begin{aligned} \theta_t^m &= \varphi(X_t^m, t) \\ X_{t+1}^m &= \lambda(\theta_t^m, u_t) \\ X_t^m &= [x_t^0, x_t^1, \ldots, x_t^m]^T \\ x_t^m &= \frac{d^m x_t}{dt^m} \end{aligned} \tag{2}$$

where $\theta_t^m \in \mathbb{R}^{1\times m}$ is the physics-informed token at timestamp t, φ denotes the encoding process, and λ represents the predicting and decoding process. The design of each module is detailed in the following.

A. Design of PITP Framework

Our PITP strategy mainly consists of data normalization, physics-informed token encoder, and dynamic decoder.

1) Data Normalization: Considering that there is high-order differentiation in the motion state, it may lead to large magnitude differences between different motion states. As a result, it will cause instability and difficulty in convergence during deep learning training. To avoid this issue, we propose scale normalization, which normalizes the data before they are input into the network

$$\begin{aligned} x_t^{\lceil m/2\rceil+1} &= x_t^{\lceil m/2\rceil} * \sqrt{d} \\ x_t^{\lceil m/2\rceil-1} &= x_t^{\lceil m/2\rceil} / \sqrt{d} \\ d &= 2\pi \max(f_{\text{train}}) \end{aligned} \tag{3}$$

where $f_{\text{train}} \in \mathbb{R}$ denotes the frequency of the train data. It is important to note that once the value of $d \in \mathbb{R}$ is determined during training, this value will be used for data normalization during actual dynamic predictions, ensuring that normalization is carried out without relying on the global data distribution.

2) Physics-Informed Token Encoder: To capture the nonlinear characteristics of the dynamics, we first develop a physics-informed encoder. In this work, we establish the encoder using a deep network [37], leveraging its ability to describe complex nonlinearities. The proposed network architecture is primarily composed of several feature processing branches, as shown in Fig. 3; each dedicated to processing features of different

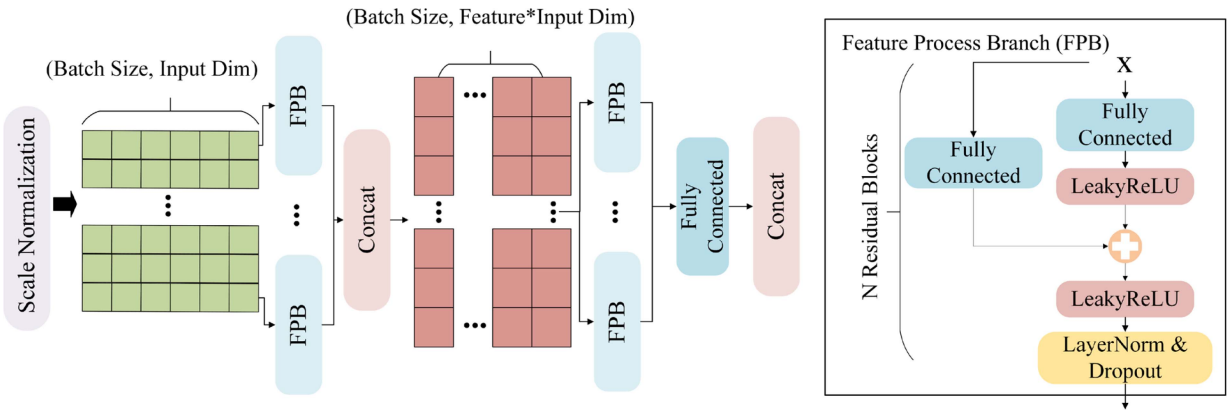

Fig. 3. Diagram of the neural network for the physics-informed token encoder.

dimensions. This ensures that diverse features undergo distinct processing, thereby facilitating a deeper exploration of the impact of the coupling of different motion states on the dynamics. Subsequently, we devise fusion and feature enhancement modules to capture the intricate couplings among system states and enhance nonlinear representation capability. Ultimately, this process generates the single value of one dimension within the output token, and several such networks collectively yield the corresponding token.

Unlike other neural networks designed for sequential processing [38], this proposed network processes single-point data and aims to learn the mapping relationship from a single-point state to a single-point token, effectively enhancing the model's inference performance. Although this approach is more challenging to train compared to data containing contextual information [39], it reduces the need for extensive high-quality data collection, as acquiring sequential data is more time-consuming.

To avoid periodic autoregressive outputs for periodic inputs that fail to capture time-dependent creep dynamics, we extend the motion state encoding with an additional time dimension to describe the time-dependent dynamic characteristics

$$\begin{aligned} \sigma_t^i &= h_i(X_t^m, t), i = 1, 2, \ldots, m \\ \theta_t^m &= [\sigma_t^1, \sigma_t^2, \ldots, \sigma_t^m] \end{aligned} \tag{4}$$

where $\theta_t^m \in \mathbb{R}^{1\times m}$ is the physics-informed token at timestamp t, and $\sigma_t^i \in \mathbb{R}$ and h_i denote the ith dimension value of the token and the network employed, respectively.

Furthermore, to ensure that the obtained tokens not only incorporate contextual dynamic state information but also possess a global perspective to capture the rate-dependent characteristics of the dynamics, we embed global physical information into the tokens. By utilizing the dynamic equations as the optimization objective and employing an unsupervised learning approach, the generated tokens are endowed with global physical information during the training process. Here, we utilize the simplified equivalent linear system to capture the global dynamic characteristics, ensuring the reversibility of the model

$$F_t = \theta_t^m X_t^m \tag{5}$$

where F_t denotes the equivalent external force. To facilitate control inversion, the external force is formulated as a quadratic function of voltage, following the relationship between Maxwell stress and the electric field intensity. Although this formulation is not strictly accurate, the resulting error can be compensated for by the physics-informed tokens on the right-hand side of the equation

$$F_t = u_t^2. \tag{6}$$

To determine the optimal order of a linear system that most accurately represents the global dynamic characteristics, we further employ system identification techniques utilizing frequency sweep response data. Moreover, the identified steady-state parameters can serve as boundaries for subsequent training, embedding additional physical knowledge into the learning process and enhancing both its stability and efficiency.

3) Dynamic Decoder: To obtain the motion state at the next time step from the physics-informed tokens, we design a dynamic decoder to predict and decode the tokens. Employing a conventional learning-based decoder would render the entire modeling process irreversible, thereby introducing new challenges for control problems. To address this issue, we directly use the simplified equivalent linear system from the encoder and treat the tokens as time-varying parameters within the linear system, which are regressed to solve the dynamics. By combining the token generated from the current state with the voltage input at the next time step, the next state can be obtained using a single-step Runge–Kutta method, effectively achieving prediction and decoding

$$\begin{aligned} \theta_t^m &= \varphi(X_t^m) \\ f_{\text{solved}} &= \left[X_t^{2:m}; \frac{u_t^2 - \theta_t^{1:m-1} X_t^{1:m-1}}{\sigma_t^m}\right] \\ X_{t+1}^m &= \text{RK4}_{\text{step}}\left(f_{\text{solved}}, X_t^m, \Delta t\right) \end{aligned} \tag{7}$$

where f_{solved} denotes the right-hand side of the ODE, and $\text{RK4}_{\text{step}}(\cdot)$ denotes the fourth-order single-step Runge–Kutta process, where the inner parameter presents the right-hand side of the ordinary differential equation (ODE), the current state vector, and the integration step size in order. This prediction process is iteratively performed in an autoregressive manner, enabling the forward-generated dynamic response to be extended indefinitely and enhancing model computational efficiency. By

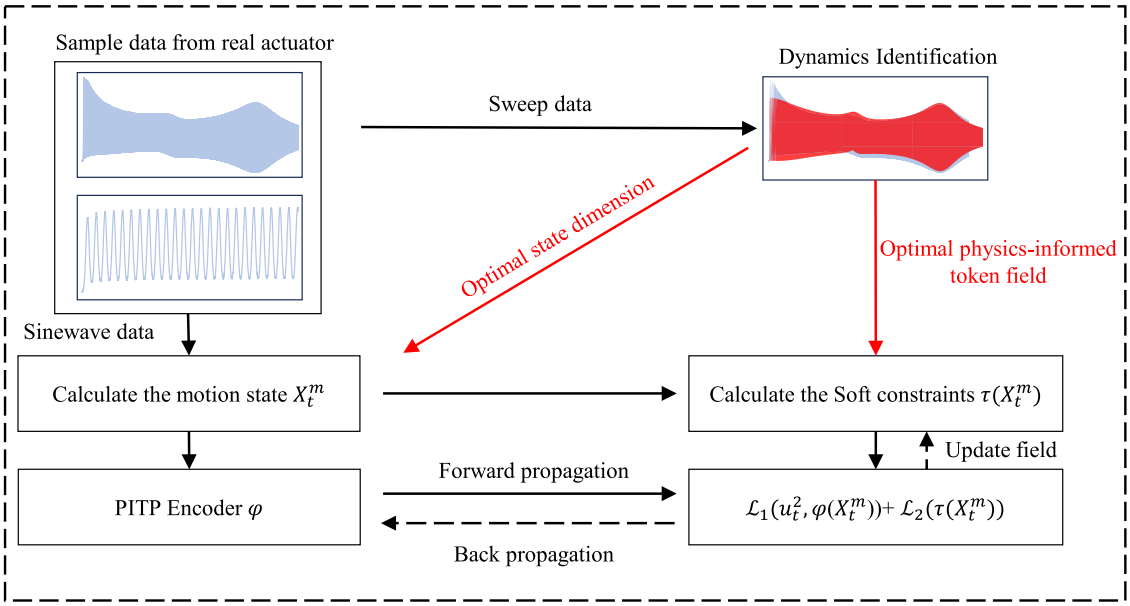

Fig. 4. Overall pipeline of the proposed hierarchical optimization training process.

leveraging state-dependent nonlinear pattern learning in token generation and dynamic decoding, this method could avoid time accumulation errors and achieve long-term prediction.

B. Data Preprocessing

To train the physics-informed encoder, we precollect the frequency sweep response data of the DEA as well as the dynamic responses to sinusoidal signals at several discrete frequency points. The frequency sweep response data containing the global dynamic behavior are used for the dynamic system identification. The sinusoidal response data, which are fed to the encoder, include the time-dependent characteristics of the output response, specifically the creep behavior. In order to obtain an m-dimensional description of the motion state, we employ a numerical differentiation method to process the acquired displacement signals

$$x_t^i = \begin{cases} \frac{x_t^{i-1} - x_{t-1}^{i-1}}{\delta t} & t = 1, T \\ \frac{x_{t+1}^{i-1} - x_{t-1}^{i-1}}{2\delta t} & t = 2, \ldots, T-1 \end{cases} \quad \text{for} \quad i = 1, \ldots, m. \tag{8}$$

To avoid the impact of experimental noise on high-order difference mutations, we employ a fourth-order low-pass Butterworth filter [40] after each differentiation step

$$H(z) = \frac{b_0 + b_1 z^{-1} + b_2 z^{-2} + b_3 z^{-3} + b_4 z^{-4}}{1 + a_1 z^{-1} + a_2 z^{-2} + a_3 z^{-3} + a_4 z^{-4}} \tag{9}$$

where $H(z)$ is the transfer function of the digital low-pass filter, and $b_0, b_1, b_2, b_3, b_4 \in \mathbb{R}$ and $a_1, a_2, a_3, a_4 \in \mathbb{R}$ are the filter coefficients. The filter coefficients are determined by the normalized cutoff frequency.

C. Hierarchical Optimization Training

Based on the previously described encoder and decoder, the details of the entire model construction process are illustrated in Fig. 4. First, the precollected data are preprocessed. Then, the sweep data are utilized to determine the basic dynamic characteristics as well as the feature dimensions m and compute the motion state X_t^m for the training data. The sinewave data are used for training the encoder. To boost training efficiency, ensure training stability, and embed the physics into the framework, a hierarchical optimization training method is introduced.

The training process typically involves comparing the error between ground truth and predicted values, and adjusting the network parameters using gradient descent methods. However, building on the previous physics-informed design, we need to integrate the physical equations as the optimization target within the encoder's optimization process. Previous studies [31] show that incorporating ODE solutions during training increases memory usage and time complexity due to the serial nature of ODE computations. In this work, we adopt the physics-informed neural networks (PINN) approach [41], directly using ODEs in the dynamic decoder as the optimization target for unsupervised training. To compare the training efficiency between the conventional supervised learning strategy involving ODE solution and the proposed unsupervised scheme, we further analyze the time complexity. Specifically, we assume the availability of a computing device capable of accommodating all data in parallel. Under this assumption, the time complexity of both methods can be expressed as follows:

$$\begin{aligned} O_{\text{supervised}} &= O(A) + O(kBT) \\ O_{\text{unsupervised}} &= O(A) \\ O_{\text{supervised}} &\propto T. \end{aligned} \tag{10}$$

From (10), the complexity is proportional to the time series length due to the serial nature of ODE computations. In addition, during backpropagation, computing the gradients of the ODE adds further time cost. Based on this, the unsupervised PINN approach offers better feature extraction under limited resources by embedding physical information directly into the encoder. However, using the equation for supervised learning may cause training oscillations, as the token and motion state are multiplicatively related in the loss function as described in the following:

$$\frac{\partial \mathcal{L}}{\partial \sigma_t^i} = W x_t^i, \sigma_t^i x_t^i \in [p, q] \tag{11}$$

where W denotes the gradient product of each layer of the neural network, and p and q are two constants near u_t^2. During backpropagation, the update to the token is scaled by the current motion state value. High-frequency motion generates larger high-order derivatives x_t^i, while the corresponding token σ_t^i should have a smaller magnitude to maintain balance. However, large gradients during tuning cause improper token updates, hindering small-range adjustments. To address this issue, we regularize the motion state by multiplying it with the corresponding coefficient from the data preprocessing of the motion state in the loss function.

During the optimization of network parameters under physical law supervision, certain generated tokens may steer the ODE solution toward a local optimum. This would introduce oscillations in the training process and result in divergence of the ODE solution. This behavior is discussed in detail in Section IV. To mitigate this issue, we introduce soft constraints into the loss function as shown in (12). The neighborhood of the dynamic equivalent constant parameters in dynamic system identification through sweep signals is used as the range for token values. While values outside this range are permitted if they lead to improved performance, they incur a penalty in the loss function. This approach balances the exploitation of parameters within a narrow range inside the defined boundaries, along with exploration beyond the range. By tuning the penalty coefficients appropriately, the model maintains its exploration potential while avoiding convergence to suboptimal solutions

$$\begin{aligned} \mathcal{L} &= \mathcal{L}_1(u_t^2, \varphi(X_t^m)) + \mathcal{L}_2(\tau(X_t^m)) \\ \mathcal{L}_1 &= \text{SmoothL1Loss}(u_t^2, \theta_t^m X_t^m) \\ \mathcal{L}_2 &= \frac{1}{m}(\alpha||\text{ReLU}(\theta_t^m - \mathbf{P})||_1 + \beta||\text{ReLU}(\mathbf{Q} - \theta_t^m)||_1) \end{aligned} \tag{12}$$

where $\mathcal{L}$ denotes the loss function, $\alpha, \beta \in \mathbb{R}$ are the penalty coefficients, $\mathbf{P}, \mathbf{Q} \in \mathbb{R}^{m\times 1}$ are the upper bound and lower bound, respectively, and τ denotes the calculation of the loss between the output token and the bounds. The boundaries are determined by enlarging and shrinking the identification results by a certain proportion.

To determine the appropriate boundaries for tuning within the defined range, we further employ a hyperparameter optimization strategy. Once the loss stabilizes after several training iterations, the tuning boundaries are expanded to explore the hyperparameter values further. The learning rate and training epochs are reduced to prevent disrupting the original learning results and prevent the model from getting stuck in a local optimum. The termination condition for tuning is that the model's loss no longer decreases after the second training epoch following each boundary expansion. The detailed training process is described in Algorithm 1.

Algorithm 1: Hierarchical Optimization Training Process.

Input: Identification result $\mathbf{y} \in \mathbb{R}^{m\times 1}$, dataset D, deep learning model φ, initial learning rate lr, training epochs n, decay factors $c < 1$, $r < 1$, boundary factors $a > 1$, $b < 1$, threshold ϵ.
Initialize $j = 0$, optimal loss $\mathcal{L}_{best} = \infty$, optimal boundary $\mathcal{B} = [0, 0]$, optimal model φ_{best}.
while $stop =$ `False` **do**
  Calculate boundary $\mathbf{Q} = b^{j+1}\mathbf{y}, \mathbf{P} = a^{j+1}\mathbf{y}$.
  for i=1 to $[n * r^j]$ **do**
    Train φ with dataset D and learning rate $lr * c^j$ and calculate loss $\mathcal{L}(D, \varphi)$ with boundary $\mathbf{P}$, $\mathbf{Q}$.
    if $\mathcal{L}_{best} - \mathcal{L} < \epsilon$ and $i > 1$ **then**
      $stop =$ `True`.
      Break.
    end if
    if $\mathcal{L} < \mathcal{L}_{best}$ **then**
      Update $\mathcal{L}_{best} = \mathcal{L}$, $\mathcal{B} = [\mathbf{Q}, \mathbf{P}]$, $\varphi_{best} = \varphi$.
    end if
  end for
end while
Save best model φ_{best} and best boundary $\mathcal{B}$.

D. Feedforward Control Strategy

Building upon the previously established dynamic model, a feedforward control strategy can be developed. As discussed in the preceding section, the developed dynamic model incorporates control requirements and adopts a relatively simple, reversible ODE formulation. Therefore, the inverse model is directly utilized as the feedforward control strategy to preplan the input voltage. Once the target trajectory and its corresponding motion state curves are computed, the motion state sequence can be directly input into the following equation to determine the required feedforward voltages:

$$\begin{aligned} \hat{\theta_t^m} &= \hat{\varphi}(\hat{X_t^m}) \\ u_t &= \text{sgn}(\hat{\theta}_t \hat{X_t^m}) \sqrt{\hat{\theta}_t \hat{X_t^m}} \end{aligned} \tag{13}$$

where $\hat{X_t^m}$ and $\hat{\theta}_t$ represent the tracking motion state and the corresponding physics-informed tokens generated by the trained model, respectively. The actuation behavior of the DEA remains unaffected by the sign of the applied voltage due to its square-law electromechanical response. To ensure mathematical consistency, we adopt the sign function to only generate positive voltage. Due to the strong nonlinear descriptive capability and simple reversible form of the dynamic model, the proposed feedforward method enables the calculation of control voltages without the need for feedback information.

III. Experiment Validation

A. Design and Fabrication of DEAs

To demonstrate the versatility of the proposed framework, we select conical DEAs under different loads and high power density DEA. The conical DEA is constructed with a single-layer acrylic elastomer, which results in large deformation and high viscoelasticity in the actuator. In contrast, the high power density DEA is made from a multilayer silicone elastomer, which leads to lower viscoelasticity, higher natural frequencies, and more intense mechanical vibrations in the actuator. The main structure and fabrication process are detailed below.

As for the fabrication of conical DEAs, it mainly consists of a prestretched elastomer membrane, compliant electrodes, and a stiff frame. The elastomer membrane (3 M VHB 4910, initial thickness: 1 mm) is equiaxially stretched at a ratio of 3, and a disk is fixed at the center of the membrane to connect the end effector (with a mass of 100, 122, or 150 g). To hold the membrane, the laser-cut frame is fabricated. The carbon grease (MG Chemical 846-80 G) is coated on both interfaces of the membrane, serving as the compliant electrodes. When the high-voltage signal is applied to the electrodes, the membrane undergoes expansion, which is constrained by the fixed frame and subsequently converted into a single-degree-of-freedom motion to drive the end effector.

The fabrication of high power density DEAs involves two main steps: 1) creating multilayer DE films and 2) roll-assembling them. A seven-layer DE film stack consists of alternating DE films (20 μm for outer layers and 40 μm for inner layers) and six electrode layers. The process begins with blade-coating a prepolymer solution (4 mm/s, 40 μm gap) onto a polyethylene terephthalate (PET) substrate, followed by degassing and curing. Patterned carbon nanotubes (CNT) electrodes (100 mm $\times$ 8 mm) are stamped onto the film. This layering repeats until seven layers are achieved. For assembly, laser-cut strips are peeled from the PET substrate. The film is soaked in ethanol and rolled onto an ethanol-coated acrylic rod (3.5 mm diameter) to form a 150-layer actuator. After drying, conductive silicone and carbon fiber plates with copper tape are applied for electrical contacts.

B. Experimental Setup

All training processes of the physics-informed token encoder and dynamic prediction procedures are conducted utilizing the PyTorch framework and are performed on a computational platform equipped with a GeForce RTX 3090 GPU and a 24-core CPU. The experiment is conducted with the experimental setup shown in Fig. 5(c). The dSPACE (dSPACE Microlab 1202) is a control module with a 16-bit analog-to-digital converter and a 16-bit digital-to-analog converter that captures the measurement signals and generates the voltage signals to the high-voltage amplifier. The high-voltage amplifier (Trek 10/10B-HS) amplifies the received control signal by a factor of 1000 and applies it to the DEA. The laser sensor (Keyence LK-H085) records the displacement of the DEA in the range of -20 to 20 mm with a sampling rate of 20 kHz. The sampling rate of the system is set to be 1 and 5 kHz for the conical DEA and the high power density DEA, respectively.

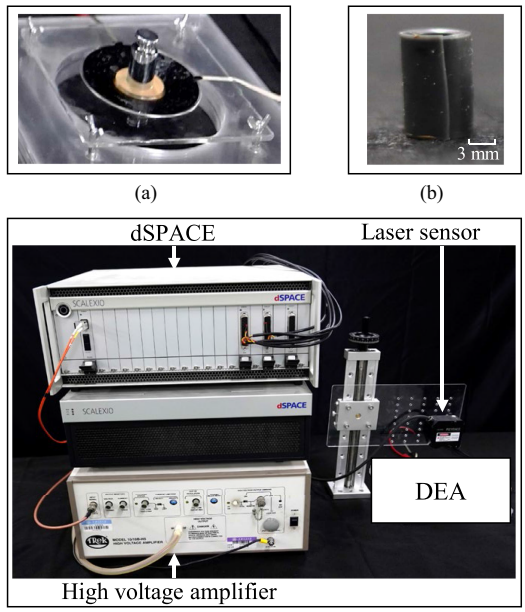

Fig. 5. Experimental setup. (a) Conical DEA. (b) High power density DEA. (c) Experiment equipment.

C. Dataset for Training

The precollected dataset for modeling is primarily divided into two parts: one consisting of frequency sweep signals with the corresponding dynamic states for dynamic system identification and the other comprising sinusoidal signals and their dynamic responses for training

$$u_{\text{sweep}} = A_1 \sin\left(\pi\left(\frac{f_{\text{end}} - f_{\text{start}}}{T}t + 2f_{\text{start}}\right)t - \frac{\pi}{2}\right) + A_2$$
$$u_{\text{sin}} = A_3 \sin\left(2\pi f t - \frac{\pi}{2}\right) + A_4 \tag{14}$$

where T denotes the lasting time of the sweep signal, and A_1 and A_3, and A_2 and A_4 are the amplitude and the offset of the signals, respectively. f_{start} and f_{end} represent the start and the end frequency of the sweep signal, respectively.

The $(f_{\text{start}}, f_{\text{end}}, T, A_1, A_2)$ is set to be (0.01 Hz, 20 Hz, 200 s, 3 kV, 3 kV) for the conical DEA and (0.01 Hz, 180 Hz, 90 s, 700 V, 700 V) for the high power density DEA. During the actual training process, to supplement the nonlinear information related to frequency and amplitude variations in the dynamics, several sets of sinusoidal signals with different amplitudes and frequencies are collected for calibration. For the conical DEA, A_3 is set to {1 kV, 2 kV, 3 kV}, and A_4 is set to be 3 kV. For each group, the sampled frequency is from 1 to 10 Hz with the 1-Hz step. For the high power density DEA, A_3 takes values from {200 V, 350 V, 500 V}, and A_4 is set to be 700 V. For each group, the sampled frequency is from 5 to 130 Hz with the 5-Hz step. The total number of subsets for the conical DEA is 30 and for the high power density DEA is 78. To avoid

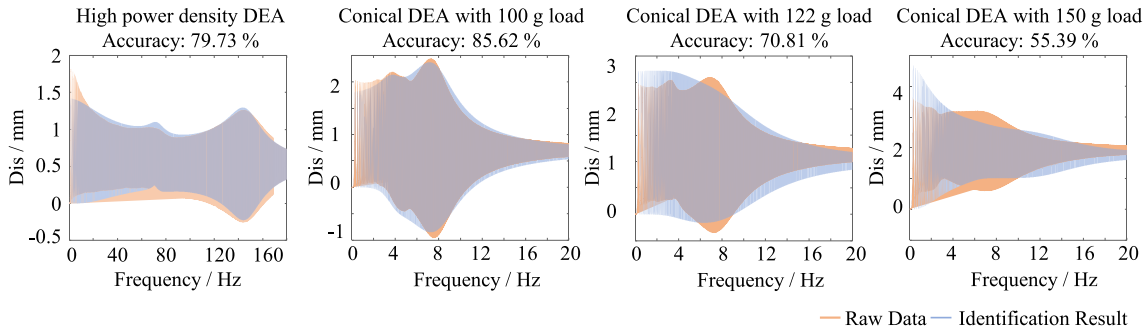

Fig. 6. Dynamic system identification results of four different configurations of DEAs. The input is the sweep signal within the working frequency interval.

measurement interference caused by heat generation from 10-s DEA motion between successive measurements, a 20-s interval is introduced between each measurement for the conical DEA and high power density DEA to ensure that the DEA returns to its original still state before the next data acquisition. Therefore, the total dataset size for the conical DEA is 900 000, while for the high power density DEA, it is 1 170 000. For each type, the data collection time does not exceed 20 min. The maximum working frequency of the DEA is determined by its mechanical structure and material. Accordingly, the operating frequencies in the experiments are selected within the feasible working range of each actuator (e.g., 10 Hz for conical DEAs and 130 Hz for the high power density DEA used in this work), as the output performance may deteriorate significantly once the frequency exceeds this limit. All subsequent dynamic modeling and control experiments are conducted within this operating range.

D. Dynamic Modeling Validation

The encoder is trained on the precollected dataset to perform dynamic prediction. The training hyperparameters are set as follows: number of steps $n = 10$, learning rate $lr = 10^{-3}$, coefficients $c = 0.8$, $r = 0.971$, $a = 1.2$, and $b = 0.8$, and penalty coefficients $\alpha = \beta = 2$. The penalty coefficients were selected by observing the relative magnitude of $\mathcal{L}_2$ with respect to $\mathcal{L}_1$ during the initial training epochs. This strategy prevents scale imbalance during optimization, thereby avoiding bias toward one objective while neglecting the other. For the model configuration, the hidden size is set to 128, the number of layers to 2, and the dropout rate to 0.4. The dynamic system identification is conducted by the tfest MATLAB function, as shown in Fig. 6. The accuracy is quantitatively characterized by the mean absolute error between the frequency sweep response of the optimally identified system and the actual physical response under the same sweep input. The optimal dimensions of the token are 3 and 4 for conical DEA and high power density DEA, respectively. When the original system is subjected to additional loads, its dynamics change, leading to reduced identification accuracy, while the optimal model order remains unchanged under these conditions. Therefore, the order of the dynamics and the system complexity are primarily determined by the material properties and configurational nonlinearities of the actuator itself. However, the nonlinearity of the neural network could still compensate for this loss. Then, the training is conducted based

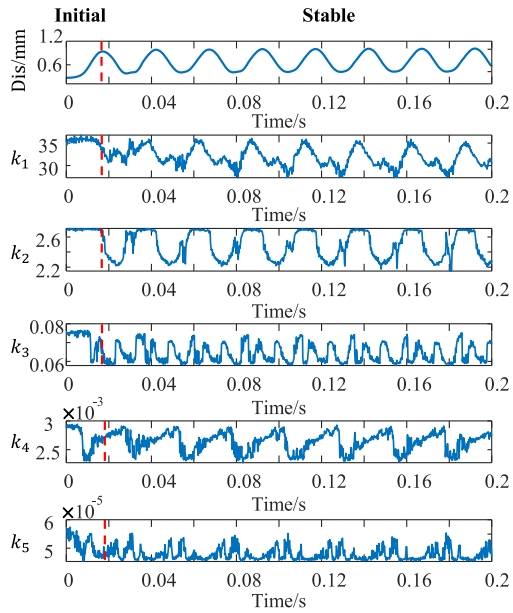

Fig. 7. Output physics-informed tokens with the trained model for the high power density DEA corresponding to the 40-Hz sine input voltages.

on the identification results, including the optimal boundaries and the optimal order of the dynamics. The training process can be paralleled through the GPU, leading to the short training time (< 5 min), occupying less than 3 GB for the high power density DEA dataset.

After training, the model generates the corresponding physics-informed token based on the initial state input. The token information from the experiment is shown in Fig. 7. On the one hand, the learned tokens in the figure exhibit periodicity, which corresponds well with the periodic sinusoidal input. On the other hand, the tokens show two distinct phases: an initial transition phase and a subsequent stable phase, aligning with the initial excitation and steady-state vibration behavior of the real motion states. It demonstrates that our training effectively embeds physical prior information and extracts dynamic characteristics. It also demonstrates that constant parameters cannot accurately describe the dynamic characteristics.

The physics-informed token along with the current input voltage is used for ODE-based decoding to predict the next motion state autoregressively. To quantitatively describe the prediction performance, the evaluation metric used here is relative

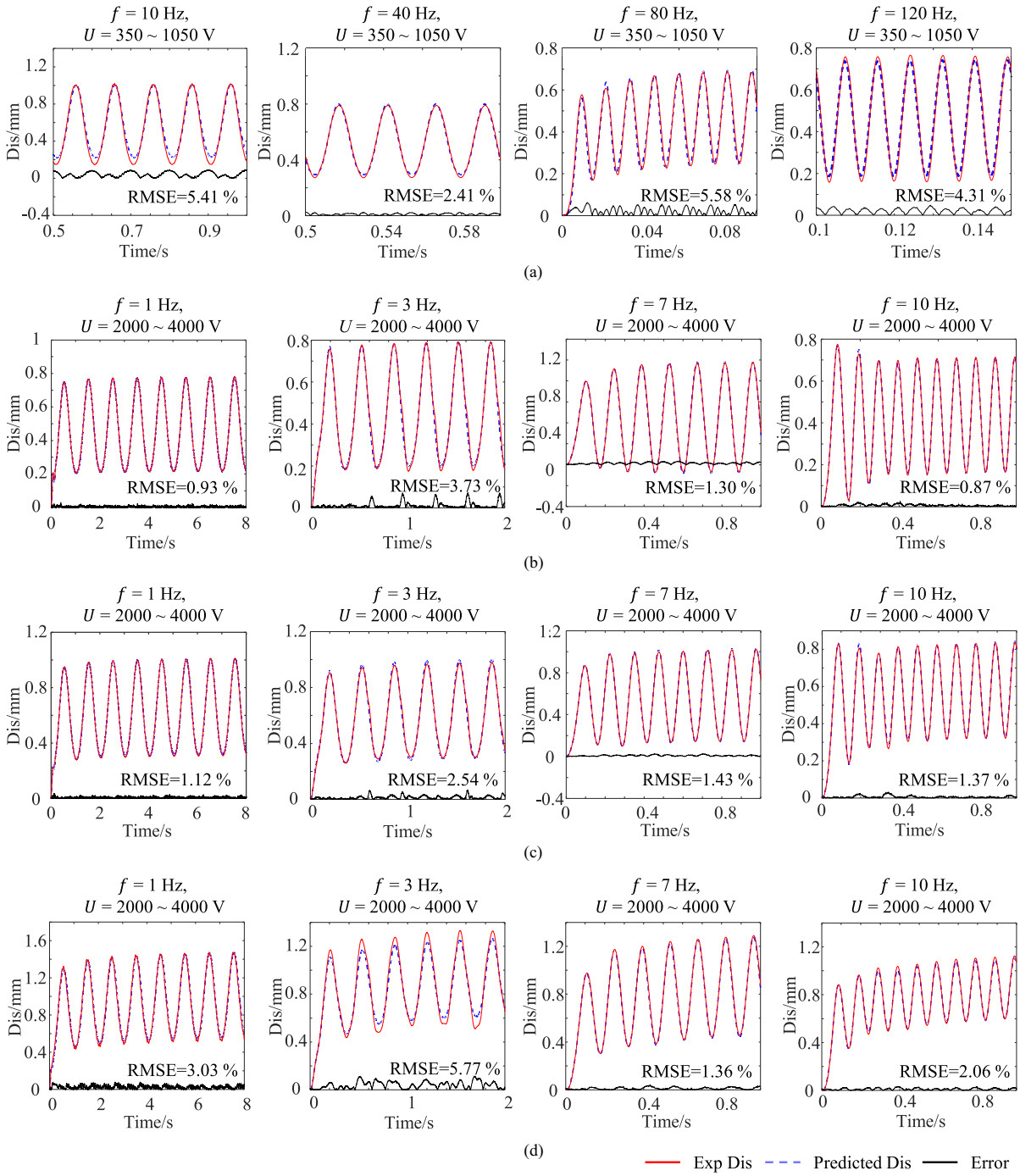

Fig. 8. Model prediction results of different DEAs at different frequencies. (a) High power density DEA. (b) Conical DEA with 100 g load. (c) Conical DEA with 122 g load. (d) Conical DEA with 150 g load.

root-mean-square error

$$e_{\text{rms}} = \frac{\sqrt{\frac{1}{N}\sum_{i=1}^{N}(x_p - x_e)^2}}{\max(x_e) - \min(x_e)} \tag{15}$$

where N is the quantity of the data, and x_e and x_p are the experimental and the predicted displacement, respectively.

The results shown in Fig. 8 illustrate the predicted outcomes for different configurations and loads at various frequencies. The natural frequencies are 3.7 and 7.4 Hz for the conical DEA with 100 g, and 68 and 142 Hz for the high power density DEA. The input waveforms are sinusoidal signals, whose value range and frequency are specified in the figure. The initial phase is $-\frac{\pi}{2}$. Our predictive experimental results show that accurate dynamic predictions can be achieved over a wider frequency range (1–130 Hz). High-frequency operation of high power density DEAs entails more complex dynamic characteristics. Achieving accurate predictions at 130 Hz demonstrates that our method

TABLE I
PREDICTION ERRORS AT DIFFERENT FREQUENCIES

DEA	High power density DEA $U = 200 - 1200\ V$		Conical DEA (100 g) $U = 1000 - 5000\ V$		Conical DEA (122 g) $U = 1000 - 5000\ V$		Conical DEA (150 g) $U = 1000 - 5000\ V$	
f/Hz	$e_{\text{rms}}/\%$	f/Hz	$e_{\text{rms}}/\%$	f/Hz	$e_{\text{rms}}/\%$	f/Hz	$e_{\text{rms}}/\%$
10	5.35	1	1.63	1	2.45	1	4.61
20	1.62	2	2.29	2	3.54	2	5.14
50	1.52	4	1.11	4	6.59	4	6.35
70	5.36	6	1.12	6	0.96	6	0.93
100	3.14	8	0.83	8	0.98	8	1.35
130	8.76	10	1.19	10	1.28	10	0.66

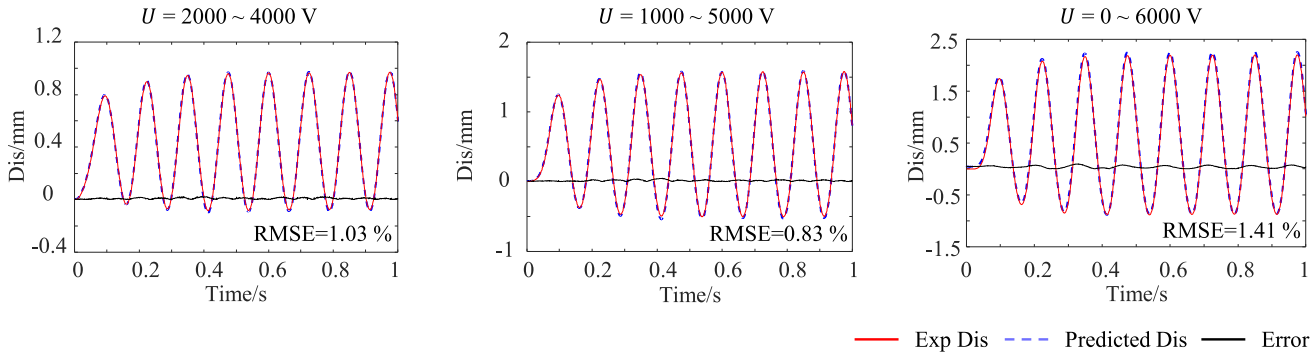

Fig. 9. Model prediction results of conical DEA with 100 g corresponding to the input 8 Hz sine waves with different amplitudes.

can effectively capture mechanical resonance, rate-dependent hysteretic viscoelasticity, and their coupled nonlinearities under high-speed operation. By embedding physical knowledge to capture global frequency-domain information and using training data to learn time-domain features, the model can efficiently utilize limited data while ensuring accurate modeling across a wide frequency range.

When the conical DEA is subjected to external loads, its natural frequency further decreases, and the resonance effect also weakens, as shown in Fig. 6. When the load is too large (such as 150 g), only a single resonance peak remains on the frequency sweep curve, and a second, larger resonance peak cannot be generated under the load. Nevertheless, as illustrated in Fig. 8, the proposed model still achieves high predictive accuracy even under such conditions. This demonstrates its powerful nonlinear modeling capability to capture severe nonlinearities induced by heavy loads. Moreover, as corroborated by the linear model identification results in Fig. 6, its accuracy does not constrain the overall performance of the proposed framework. The network complements the unmodeled nonlinear dynamics through learning-based tokens, effectively compensating for these discrepancies by leveraging its strong nonlinear fitting capability. These results collectively verify that the proposed modeling framework maintains high predictive accuracy across DEAs with substantially different geometries, materials, and structural configurations, demonstrating strong cross-configuration generality.

The detailed results can refer to Table I. The corresponding amplitudes of the input signals range from 1000 to 5000 V for the conical DEA and from 200 to 1200 V for the high power density DEA. High-precision predictions across different configurations

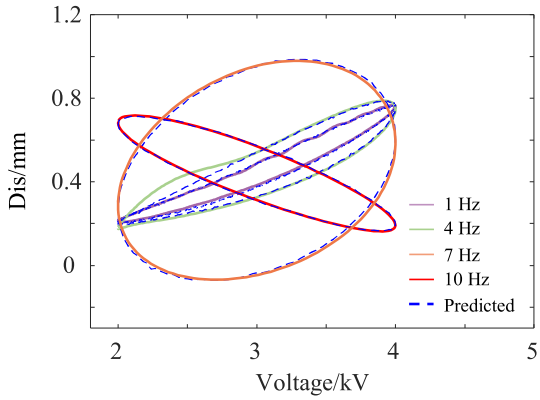

Fig. 10. Hysteresis loop prediction results for the conical DEA with 100 g load.

in a wide band are achieved, validating the versatility of our model. The proposed model combines simplicity with powerful descriptive capability, effectively overcoming this limitation and providing a solid foundation for feedforward control. Furthermore, we test the model's ability to describe the nonlinearity of amplitude variations, as shown in Fig. 9.

Meanwhile, Fig. 10 is an example demonstrating that the proposed model can accurately predict the hysteresis loop and describe rate-dependent hysteresis. This is beneficial when inverting the model for control, as it allows for the direct elimination of rate-dependent hysteresis nonlinearities.

A comparative experiment is further conducted between our model and the existing wide-band general dynamic models for control [26], [42]. The trajectories in Fig. 11 were included in the training set, and the comparative methods were trained and

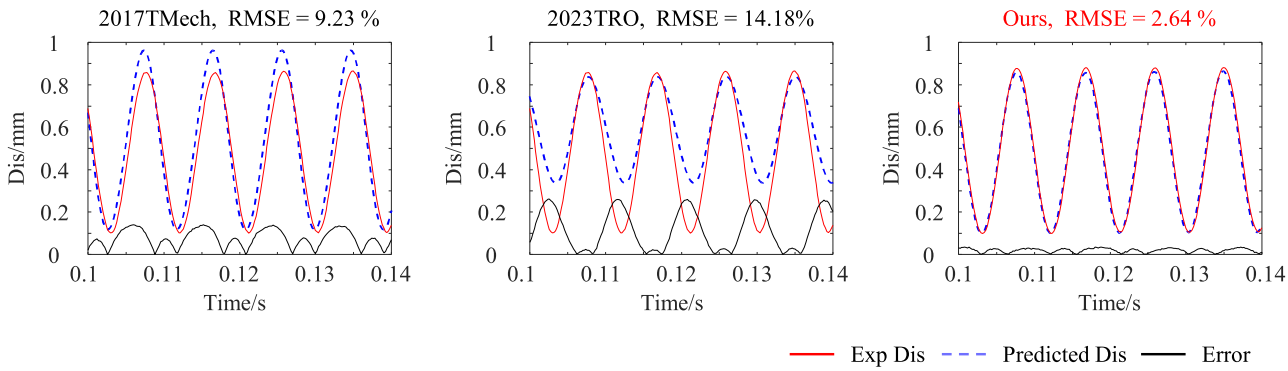

Fig. 11. Model prediction results at 110 Hz for the high power density DEA using different methods.

TABLE II
TRACKING ERRORS AT DIFFERENT FREQUENCIES

DEA	High power density DEA		Conical DEA (100 g)		Conical DEA (122 g)		Conical DEA (150 g)
f/Hz	$e_{\text{rms}}/\%$	f/Hz	$e_{\text{rms}}/\%$	f/Hz	$e_{\text{rms}}/\%$	f/Hz	$e_{\text{rms}}/\%$
10	4.70	1	6.48	1	6.56	1	4.61
30	4.24	4	8.19	4	2.89	4	6.20
90	8.35	7	9.89	7	9.33	7	18.45
130	8.55	10	11.38	10	5.75	10	12.18

executed using the same data, ensuring a fair and consistent comparison. The results shown in Fig. 11 demonstrate that existing methods are unable to provide accurate dynamic predictions at high frequencies—particularly in the case of high power density DEAs, where dynamic coupling and vibrational modes become significant. These results suggest that our proposed approach may offer a potentially useful alternative for modeling DEAs in high-frequency operating regimes.

E. Control Experiment

Based on the established dynamic model, we can directly invert it for feedforward control of the DEA. Under our experimental configuration, generating 120 000 feedforward voltage values required approximately 28.29 ms for the neural network computation and 0.61 ms for the inverse model computation. To verify the effectiveness of the inversion method, we first conducted validation in simulation. As shown in Fig. 12(a), the inverted voltage curve exhibits a clear creep-compensating trend. This voltage sequence was then input into the original forward model. Fig. 12(b) shows the small error between the desired displacement and the simulated displacement, which corresponds to the voltage generated from the desired displacement. It demonstrates the effectiveness of the proposed inversion method for feedforward voltage generation. It also demonstrates the capability of the proposed method to generate long-horizon control sequences and achieve long-term prediction. The voltages obtained from the inversion are applied to the actual actuator for feedforward control without adaptation, and the tracking results are shown in Fig. 13. The detailed results are listed in Table II. This indicates that our feedforward control can achieve high-precision trajectory tracking at different frequencies without error feedback. Its generality is further validated

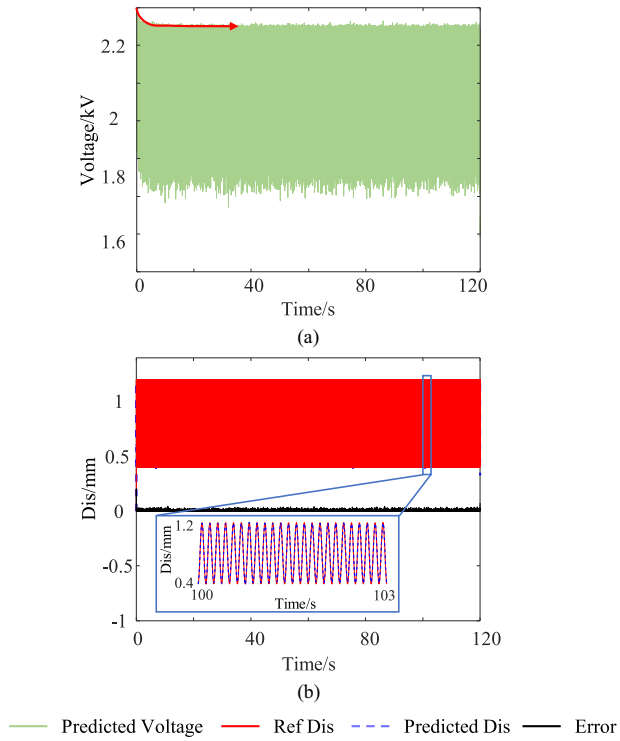

Fig. 12. Long-time prediction results of conical DEA with 100 g at 8 Hz. (a) Generated voltages. (b) Predicted displacements of generated voltages.

by the consistent performance observed across actuators with different configurations. This simple inversion method enables accurate trajectory tracking, further confirming that the proposed approach can effectively describe the real dynamic characteristics. It is worth noting that the tracking accuracy exhibits a

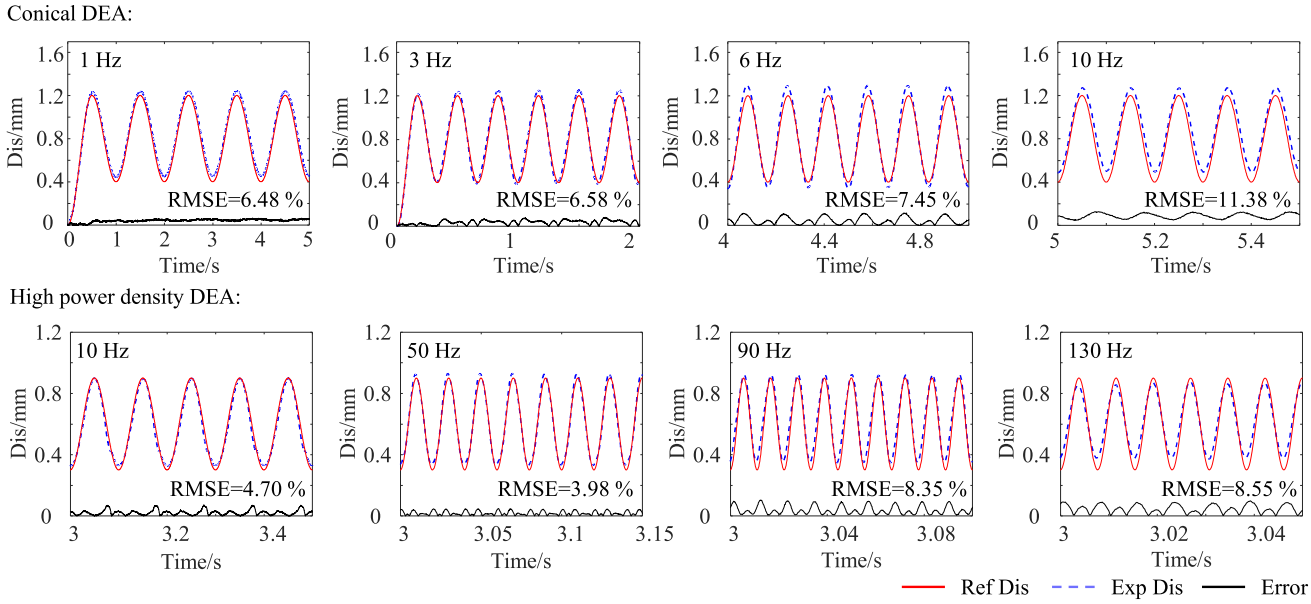

Fig. 13. Experimental results at different frequencies of the conical DEA with 100 g load and high power density DEA through feedforward control.

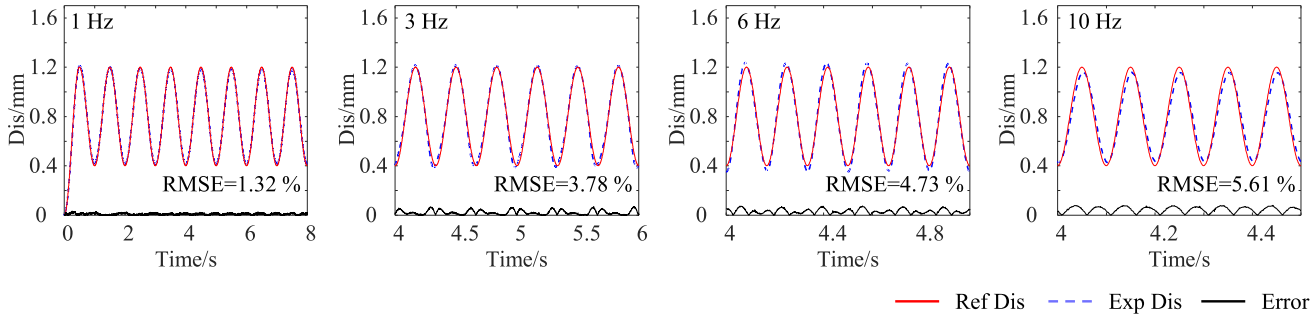

Fig. 14. Experimental results at different frequencies of the conical DEA with 100 g load through feedforward control and PI controller.

slight decline at higher frequencies, especially near 130 Hz. This behavior can be attributed to the approach toward the upper boundary of the trained frequency range in combination with the amplification of model uncertainties under high-dynamic conditions.

In the open-loop control results for the conical DEA, the error increases significantly with the increase in frequencies. The control error may arise from the time-varying nature of the DEA, model uncertainties, measurement errors, and the shift in the DEA's equilibrium position. This is further evidenced by the noticeable deviation of the average error trend. To further compensate for the steady-state offset, the PI controller ($P = 0.1, I = 0.3$) is utilized on top of the original open-loop sequence, and the results are shown in Fig. 14. The results show that the steady-state error is significantly reduced, and the motion control accuracy is further improved. This result further indicates that the observed error does not originate from the inherent nonlinearity of the DEA dynamics, since a PI controller alone is incapable of compensating for rate-dependent viscoelasticity [43]. It demonstrates that the proposed feedforward control strategy effectively compensates for the nonlinear dynamic characteristics of the DEA.

To further verify the control strategy's generality, we conduct trajectory tracking on a conical DEA with different constant loads (see Fig. 15). Despite significant changes in dynamic characteristics due to the added load, the method still accurately models the dynamics through training, generating effective feedforward control voltages. To quantitatively describe the extent of hysteresis, we further introduce the relative maximum hysteresis error (RMHE) metric [44]

$$e_{\text{rmhe}} = \max\left(\left|\frac{e_{\text{mhe}}(x_e)}{\max(x_r) - \min(x_r)}\right|\right)$$
$$e_{\text{mhe}}(x_e) = \max(x_r(x_e)) - \min(x_r(x_e)), (f_C(x_e, x_r) \le 0) \tag{16}$$

where e_{mhe} denotes the maximum vertical difference of the points inside the hysteresis loop. f_C represents the enclosed hysteresis loop. x_e and x_r are the experimental and the reference displacement, respectively. The results in Fig. 16 illustrate the hysteresis loops at different frequencies after compensation by feedforward control. It demonstrates that the proposed method effectively compensates for the rate-dependent hysteresis of the DEAs, achieving a linearized relationship between the actual

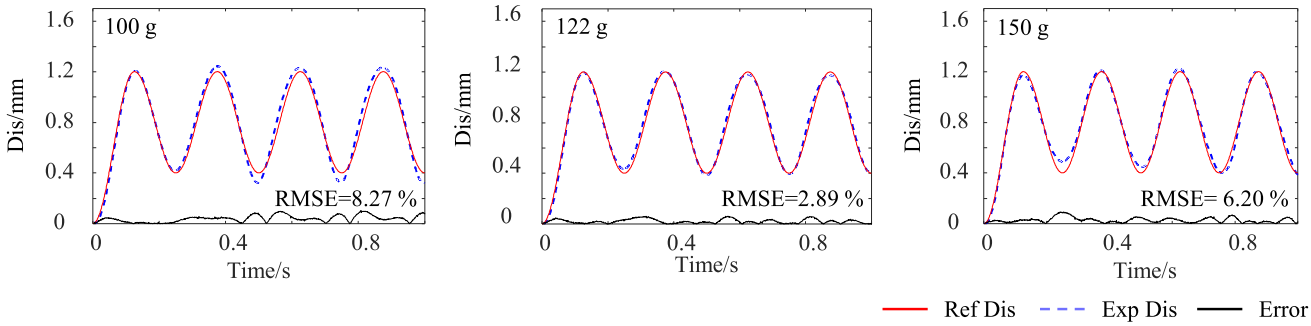

Fig. 15. Experimental results of trajectory tracking for the conical DEAs with different constant loads through proposed feedforward control strategy.

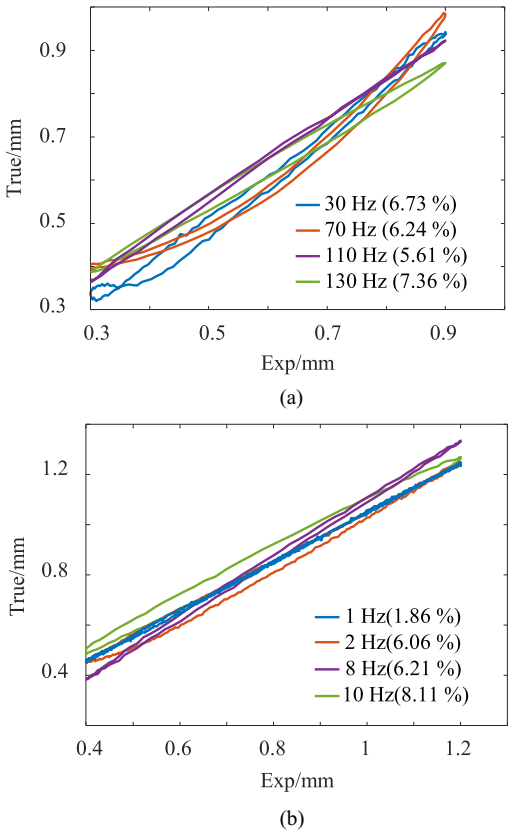

Fig. 16. Compensated hysteresis loop of the DEAs through feedforward control within one cycle. The percentage values in the figure represent the RMHE of the corresponding hysteresis loops. (a) High power density DEA. (b) Conical DEA with 100 g load.

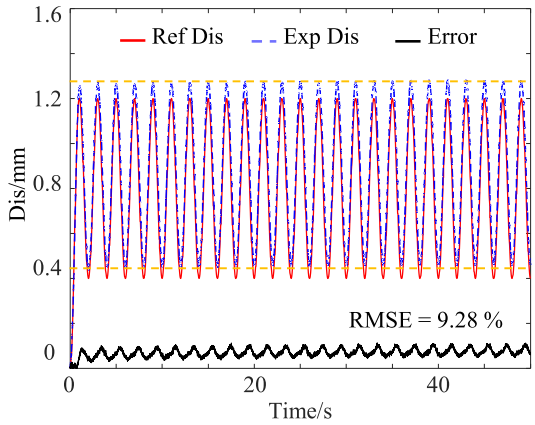

Fig. 17. Tracking result of a 50-s duration of the conical DEA with 100 g load through the proposed feedforward control at 0.5 Hz.

displacement output and the desired input trajectory. In addition, Fig. 17 presents the sine trajectory tracking performance over a 50-s duration. Throughout the tracking process, the displacement error remains consistently bounded without noticeable drift or accumulation, providing strong evidence that the open-loop model successfully compensates for viscoelastic creep effects even in the absence of real-time sensor feedback.

To further evaluate the generalization capability enabled by our physics-informed framework, we conducted tracking experiments on complex trajectories featuring waveforms, frequencies, and amplitudes absent from the training set. As shown in Fig. 18, the feedforward voltages—generated directly by the trained inverse model without additional adaptation—achieve precise compensation and accurate tracking across varying motion ranges and speeds. This capability confirms effective control over unseen trajectories. More importantly, such performance demonstrates that embedding global frequency-domain dynamics as physical constraints during token initialization enables generalization beyond the training data, thereby reducing the model's reliance on exhaustive data.

IV. Discussion

In this section, we further conduct the ablation study to investigate the effect of scale normalization, dynamic system identification, and soft constraints. We define the three variants of the PITP-based dynamic model. 1) *No limit:* The original algorithm architecture remains unchanged, with the regularization term τ on the training range $\mathbf{P}$, $\mathbf{Q}$ removed from the loss function. 2) *No scale:* The original algorithm architecture remains unchanged, with no $\sqrt{d}$ normalization applied to the training data before they are input into the network. The ablation study is conducted on the conical DEA with 100 g load dataset.

The loss curve during the training process is shown in Fig. 19. The *No scale* method exhibits a large loss during the initial training, failing to converge quickly, and the loss remains at a relatively high value upon convergence. This is due to the large

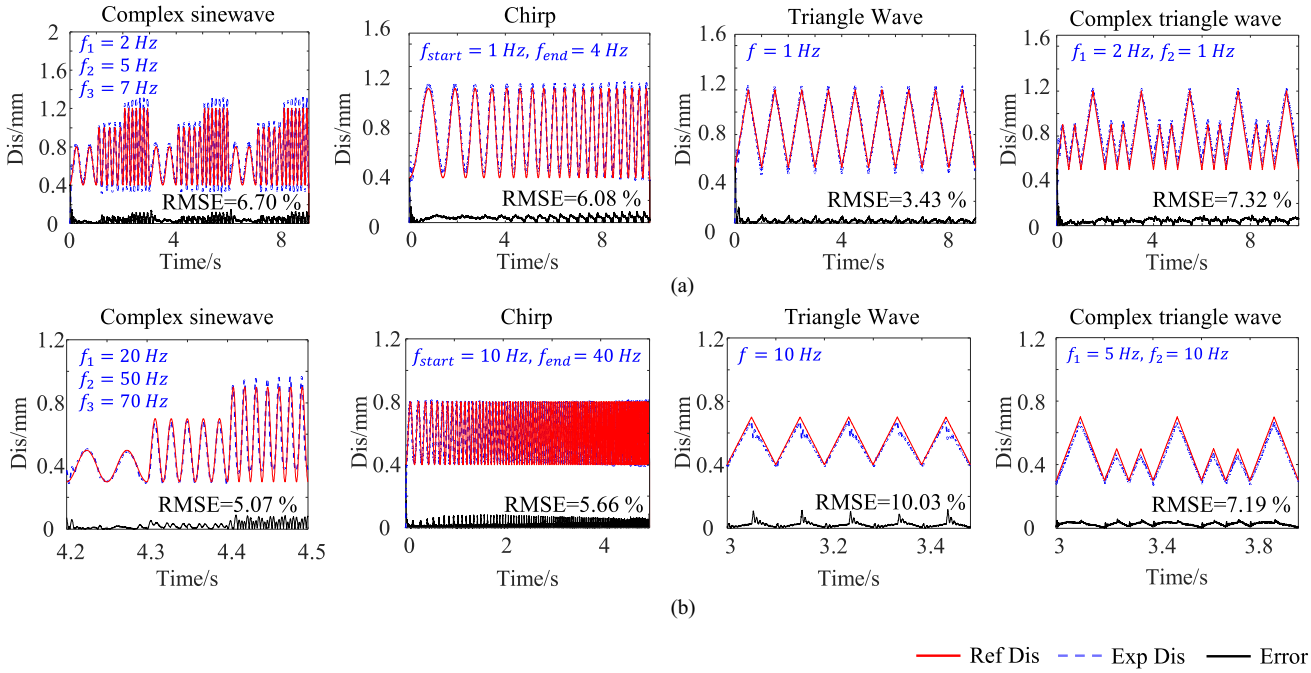

Fig. 18. Experimental results of tracking complex trajectories through proposed feedforward control strategy. (a) Results of the conical DEA with 100 g load. (b) Results of the high power density DEA.

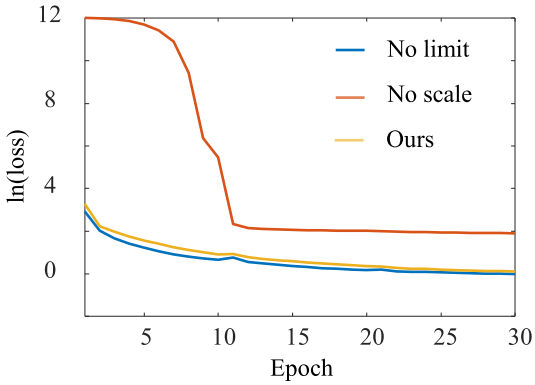

Fig. 19. Training loss curves of the proposed method and its two variants.

magnitude of the motion state, which causes the tuning step to exceed the range of the token itself. As a result, the product term in the entire supervised equation becomes much larger than u_t^2, causing the gradient descent process to fail. It further validates that the proposed "scale" method effectively facilitates rapid convergence during training and prevents training failure caused by gradients exceeding the allowable range of the tokens. However, it is important to note that standard normalization methods employed in conventional training strategies, including min–max and z-score, are not suitable in this case. This is because, during prediction, the global distribution of the dynamic states is unknown, preventing reliable estimation of the data range. The proposed scale normalization method can address this issue. Although this method cannot precisely normalize signals across all frequencies to a more consistent range, it effectively ensures that the predicted data remain within the same order of magnitude to improve the training effectiveness, which is validated in the study.

Fig. 20 shows the prediction results of the models trained using three different methods at 3 Hz. The *No scale* method fails to converge to the correct optimal range, as the large token values lead to divergence when solving the ODE to predict the dynamic curve. This results in the model's prediction deviating significantly from the expected dynamic behavior. For the *No limit* variant, this approach corresponds to the conventional deep neural network training method, where network weights are freely optimized. As shown in the results, the initial phase of prediction closely follows the dynamic curve, indicating accurate early-stage estimation. However, as the prediction proceeds, the dynamic behavior gradually drifts, and the accuracy deteriorates. This occurs because, without soft constraints, the model outputs are no longer bounded. Consequently, even small deviations between the predicted and actual motion states can produce inaccurate tokens. These tokens then propagate through the system, causing the model output to diverge at certain points and ultimately resulting in poor predictions. This further underscores the importance of incorporating soft constraints into the model. The proposed soft constraints serve to embed physical prior knowledge, ensuring that the model's predictions stay within reasonable bounds. By constraining the outputs to a certain degree, these constraints enhance the model's ability to converge and maintain accuracy throughout the prediction process, highlighting their essential role in improving model stability and predictive performance.

To further validate the importance of physical prior knowledge in the model, we replace the optimal dynamic system identification part of the model with a simple identified second-order dynamic system. After training, the results obtained by

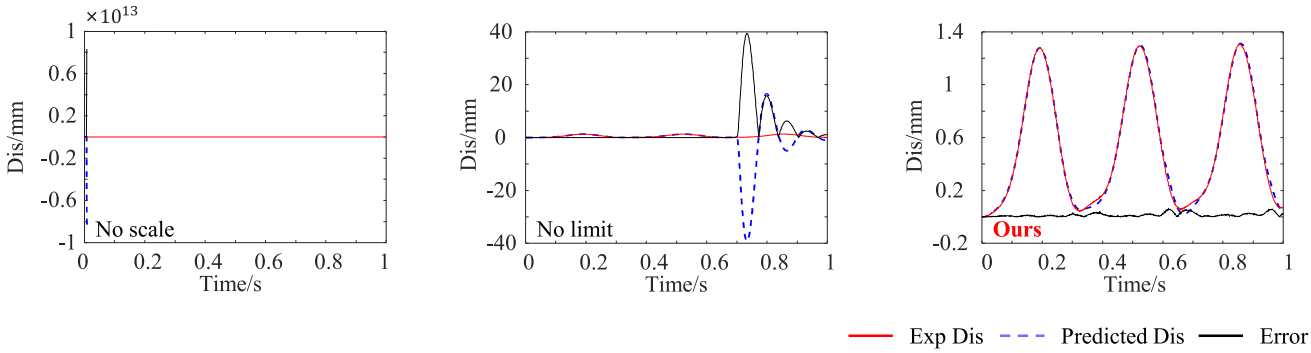

Fig. 20. Prediction results at 3 Hz through the proposed method and its two variants.

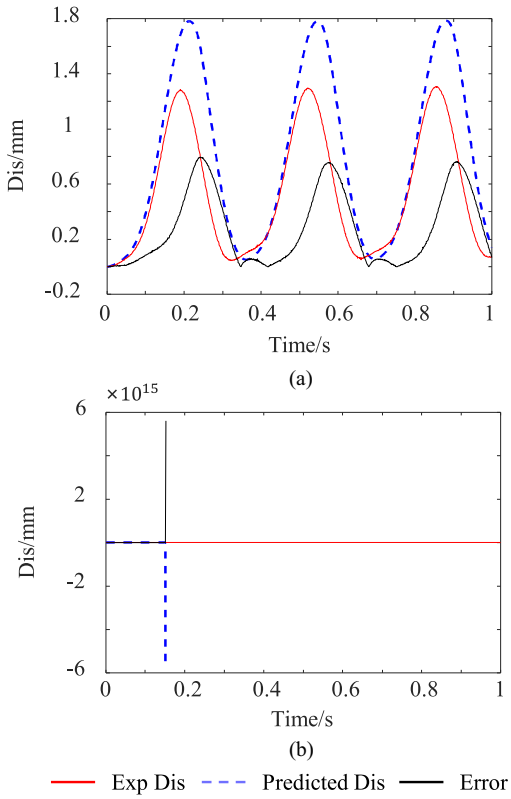

Fig. 21. Prediction results of the conical DEA with 100 g load through the proposed method with second-order dynamic system identification instead of the optimal dynamic system identification. (a) 3 Hz. (b) 5 Hz.

testing the model in this scenario are shown in Fig. 21. Despite the powerful nonlinear capabilities of the neural network, the second-order dynamic system still fails to accurately describe certain frequencies. It further illustrates that a mismatched physical architecture can lead to the failure of the method, thereby validating the necessity of embedding optimal dynamic system identification within the approach.

Benefiting from the effective integration of global physical priors and data-based learning approaches, our method can accomplish complex dynamic modeling tasks in a short time, providing the possibility of broadening the application of DEAs. The proposed framework enables rapid data collection and efficient training, which is particularly advantageous for modeling and controlling nonstandardized DEA devices. Moreover, the simple feedforward control strategy developed upon this framework ensures accurate control performance without relying on real-time sensor feedback, thereby simplifying hardware requirements and extending potential deployment scenarios.

It should be noted that this work mainly adopts a feedforward control strategy to verify the effectiveness of our dynamic models. As a result, it may suffer from deteriorated performance under varying loads, external disturbances, or continuously changing operating conditions. In our future work, we will focus on incorporating closed-loop strategies on top of the proposed model to enable robust adaptation to varying task conditions and to further extend its practical applicability. Leveraging the high computational efficiency of our inverse feedforward voltage design, we intend to implement the algorithm in the real-time control system to support sustained long-duration tracking control. Moreover, when DEAs undergo stiffness degradation or fatigue, the current model may become invalid. In such cases, embedding a fatigue-damage model into the framework could help extend the effective control lifespan of DEAs and broaden the range of potential applications. This direction will also be included in our future work. In addition, the applicability of this method may provide a feasible approach for modeling single-input-single-output nonlinear dynamic systems, although this versatility still requires further validation. Moreover, extending the framework to multi-input-multi-output systems with cross-coupled nonlinearities has not yet been addressed and remains an open challenge. In future work, it would also be worthwhile to incorporate additional physical quantities, such as temperature, pressure, or velocity, which may influence the physical properties of the material [45]. It may further enhance the model's adaptability and multitasking capability.

V. Conclusion

In this work, we propose a PITP framework for dynamic modeling and feedforward control of DEA. The dynamic process is decomposed by encoding, predicting, and decoding the physics-informed tokens. First, the neural network encoder is established through the precollected dynamic response data. Then, the sweep data are utilized to identify the simplified

equivalent linear model, which contains the global dynamic characteristics. By integrating dynamic system identification results for unsupervised learning of the encoder, we improve training efficiency and embed physical prior into tokens. A hierarchical optimization training strategy is further applied, gradually adjusting the physical boundaries to balance parameter exploration and training stability. Once trained, the physics-informed tokens can be autoregressively solved for dynamic model prediction and used to calculate the inverse model for feedforward control. Experimental results of several DEAs with different configurations and payloads demonstrate that the invertible dynamic model can precisely describe the nonlinear dynamic characteristics of the DEAs and be used for the accurate high-speed feedforward tracking control of different trajectories. In addition, the low time cost of the general dynamic model establishment further validates the effectiveness and versatility of the proposed framework.

ACKNOWLEDGMENT

Thanks to *openbayes.com* for providing the computing resources.

REFERENCES

[1] R. Pelrine, R. Kornbluh, Q. Pei, and J. Joseph, "High-speed electrically actuated elastomers with strain greater than 100%," *Science*, vol. 287, no. 5454, pp. 836–839, 2000.

[2] G. Gu, J. Zhu, L. M. Zhu, and X. Zhu, "A survey on dielectric elastomer actuators for soft robots," *Bioinspiration Biomimetics*, vol. 12, no. 1, 2017, Art. no. 011003.

[3] E. Hajiesmaili and D. R. Clarke, "Dielectric elastomer actuators," *J. Appl. Phys.*, vol. 129, no. 15, 2021, Art. no. 151102.

[4] B. Chen et al., "All-solid ionic eye," *J. Appl. Mechan.*, vol. 88, no. 3, 2021, Art. no. 031016.

[5] G. Berselli, R. Vertechy, G. Vassura, and V. Parenti-Castelli, "Optimal synthesis of conically shaped dielectric elastomer linear actuators: Design methodology and experimental validation," *IEEE/ASME Trans. Mechatron.*, vol. 16, no. 1, pp. 67–79, Feb. 2011.

[6] B. O'Brien, T. McKay, E. Calius, S. Xie, and I. Anderson, "Finite element modelling of dielectric elastomer minimum energy structures," *Appl. Phys. A*, vol. 94, pp. 507–514, 2009.

[7] H. Zhao, A. M. Hussain, M. Duduta, D. M. Vogt, R. J. Wood, and D. R. Clarke, "Compact dielectric elastomer linear actuators," *Adv. Funct. Mater.*, vol. 28, no. 42, 2018, Art. no. 1804328.

[8] G. Kovacs, L. Düring, S. Michel, and G. Terrasi, "Stacked dielectric elastomer actuator for tensile force transmission," *Sensors Actuators A: Phys.*, vol. 155, no. 2, pp. 299–307, 2009.

[9] G. Gu, J. Zou, R. Zhao, X. Zhao, and X. Zhu, "Soft wall-climbing robots," *Sci. Robot.*, vol. 3, no. 25, 2018, Art. no. eaat2874.

[10] Y. Chen et al., "Controlled flight of a microrobot powered by soft artificial muscles," *Nature*, vol. 575, no. 7782, pp. 324–329, 2019.

[11] G. Li et al., "Self-powered soft robot in the Mariana Trench," *Nature*, vol. 591, no. 7848, pp. 66–71, 2021.

[12] H. Zhao et al., "A wearable soft haptic communicator based on dielectric elastomer actuators," *Soft Robot.*, vol. 7, no. 4, pp. 451–461, 2020.

[13] G. Gu, U. Gupta, J. Zhu, L. M. Zhu, and X. Zhu, "Modeling of viscoelastic electromechanical behavior in a soft dielectric elastomer actuator," *IEEE Trans. Robot.*, vol. 33, no. 5, pp. 1263–1271, Oct. 2017.

[14] C. Cao, L. Chen, T. L. Hill, L. Wang, and X. Gao, "Exploiting bistability for high-performance dielectric elastomer resonators," *IEEE/ASME Trans. Mechatron.*, vol. 27, no. 6, pp. 5994–6005, Dec. 2022.

[15] S. Jiang, C. Tang, X. Dong, X.-J. Liu, and H. Zhao, "Soft pocket pump for multi-medium transportation via an active tubular diaphragm," *Adv. Funct. Mater.*, vol. 33, no. 50, 2023, Art. no. 2305289.

[16] L.-J. Yin et al., "A high-response-frequency bimodal network polyacrylate elastomer with ultrahigh power density under low electric field," *Nature Commun.*, vol. 15, no. 1, 2024, Art. no. 9819.

[17] Z. Suo, X. Zhao, and W. H. Greene, "A nonlinear field theory of deformable dielectrics," *J. Mechan. Phys. Solids*, vol. 56, no. 2, pp. 467–486, 2008.

[18] Z. Suo, "Theory of dielectric elastomers," *Acta Mechanica Solida Sinica*, vol. 23, no. 6, pp. 549–578, 2010.

[19] X. Zhang, Y. Liu, X. Chen, Z. Li, and C.-Y. Su, "Adaptive pseudoinverse control for constrained hysteretic nonlinear systems and its application on dielectric elastomer actuator," *IEEE/ASME Trans. Mechatron.*, vol. 28, no. 4, pp. 2142–2154, Aug. 2023.

[20] Y. Wang, X. Zhang, Z. Li, X. Chen, and C.-Y. Su, "Adaptive implicit inverse control for a class of butterfly-like hysteretic nonlinear systems and its application to dielectric elastomer actuators," *IEEE Trans. Ind. Electron.*, vol. 70, no. 1, pp. 731–740, Jan. 2023.

[21] J. Zou and G. Gu, "Modeling the viscoelastic hysteresis of dielectric elastomer actuators with a modified rate-dependent Prandtl–Ishlinskii model," *Polymers*, vol. 10, no. 5, 2018, Art. no. 525.

[22] J. Zou and G. Gu, "Feedforward control of the rate-dependent viscoelastic hysteresis nonlinearity in dielectric elastomer actuators," *IEEE Robot. Autom. Lett.*, vol. 4, no. 3, pp. 2340–2347, Jul. 2019.

[23] P. Huang, J. Wu, P. Zhang, Y. Wang, and C. Y. Su, "Dynamic modeling and tracking control for dielectric elastomer actuator with a model predictive controller," *IEEE Trans. Ind. Electron.*, vol. 69, no. 2, pp. 1819–1828, Feb. 2022.

[24] X. Zhang, H. Xu, X. Chen, Z. Li, and C.-Y. Su, "Modeling and adaptive output feedback control of butterfly-like hysteretic nonlinear systems with creep and their applications," *IEEE Trans. Ind. Electron.*, vol. 70, no. 5, pp. 5182–5191, May 2023.

[25] G. Rizzello, D. Naso, A. York, and S. Seelecke, "Modeling, identification, and control of a dielectric electro-active polymer positioning system," *IEEE Trans. Control Syst. Technol.*, vol. 23, no. 2, pp. 632–643, Mar. 2015.

[26] J. Zou, S. O. Kassim, J. Ren, V. Vaziri, S. S. Aphale, and G. Gu, "A generalized motion control framework of dielectric elastomer actuators: Dynamic modeling, sliding-mode control and experimental evaluation," *IEEE Trans. Robot.*, vol. 40, pp. 919–935, 2024.

[27] T. Hoffstadt and J. Maas, "Adaptive sliding-mode position control for dielectric elastomer actuators," *IEEE/ASME Trans. Mechatron.*, vol. 22, no. 5, pp. 2241–2251, Oct. 2017.

[28] G. Rizzello, D. Naso, B. Turchiano, and S. Seelecke, "Robust position control of dielectric elastomer actuators based on LMI optimization," *IEEE Trans. Control Syst. Technol.*, vol. 24, no. 6, pp. 1909–1921, Nov. 2016.

[29] Z. Ye and Z. Chen, "Modeling and control of a 2-DOF dielectric elastomer diaphragm actuator," *IEEE/ASME Trans. Mechatron.*, vol. 24, no. 1, pp. 218–227, Feb. 2019.

[30] J. Zou, J. D. MacLean, J. Ren, S. S. Aphale, and G. Gu, "Proxy-based sliding-mode tracking control of dielectric elastomer actuators through eliminating rate-dependent viscoelasticity," *Smart Mater. Structures*, vol. 31, no. 10, 2022, Art. no. 104002.

[31] X. Chen, J. Ren, G. Gu, and J. Zou, "Dynamic model based neural implicit embedded tracking control approach for dielectric elastomer actuators with rate-dependent viscoelasticity," *IEEE Robot. Autom. Lett.*, vol. 9, no. 10, pp. 9031–9038, Oct. 2024.

[32] Y. Zhang, J. Wu, P. Huang, C. Y. Su, and Y. Wang, "Inverse dynamics modelling and tracking control of conical dielectric elastomer actuator based on GRU neural network," *Eng. Appl. Artif. Intell.*, vol. 118, 2023, Art. no. 105668.

[33] H. Xiao, J. Wu, W. Ye, and Y. Wang, "Dynamic modeling for dielectric elastomer actuators based on LSTM deep neural network," in *Proc. 5th Int. Conf. Adv. Robot. Mechatron.*, 2020, pp. 119–124.

[34] P. Huang, J. Wu, Q. Meng, Y. Wang, and C.-Y. Su, "Self-sensing motion control of dielectric elastomer actuator based on NARX neural network and iterative learning control architecture," *IEEE/ASME Trans. Mechatron.*, vol. 29, no. 2, pp. 1374–1384, Apr. 2024.

[35] S. Borgeaud et al., "Improving language models by retrieving from trillions of tokens," in *Proc. Int. Conf. Mach. Learn.*, 2022, pp. 2206–2240.

[36] J. Devlin, M.-W. Chang, K. Lee, and K. Toutanova, "BERT: Pre-training of deep bidirectional transformers for language understanding," in *Proc. 2019 Conf. North Amer. chapter Assoc. Comput. Linguistics: Hum. Lang. Technol.*, 2019, pp. 4171–4186.

[37] A. Vaswani et al., "Attention is all you need," in *Proc. 31st Int. Conf. Neural Inf. Process. Syst.*, 2017, pp. 6000–6010.

[38] M. Liu et al., "SCINet: Time series modeling and forecasting with sample convolution and interaction," in *Proc. 36th Int. Conf. Neural Inf. Process. Syst.*, 2022, pp. 5816–5828.

[39] Y. Bengio, R. Ducharme, P. Vincent, and C. Jauvin, "A neural probabilistic language model," *J. Mach. Learn. Res.*, vol. 3, pp. 1137–1155, 2003.

[40] S. Butterworth et al., "On the theory of filter amplifiers," *Wireless Engineer*, vol. 7, no. 6, pp. 536–541, 1930.
[41] M. Raissi, P. Perdikaris, and G. E. Karniadakis, "Physics-informed neural networks: A deep learning framework for solving forward and inverse problems involving nonlinear partial differential equations," *J. Comput. Phys.*, vol. 378, pp. 686–707, 2019.
[42] S. Hau, G. Rizzello, M. Hodgins, A. York, and S. Seelecke, "Design and control of a high-speed positioning system based on dielectric elastomer membrane actuators," *IEEE/ASME Trans. Mechatron.*, vol. 22, no. 3, pp. 1259–1267, Jun. 2017.
[43] J. Zou and G. Gu, "High-precision tracking control of a soft dielectric elastomer actuator with inverse viscoelastic hysteresis compensation," *IEEE/ASME Trans. Mechatron.*, vol. 24, no. 1, pp. 36–44, Feb. 2019.
[44] G. Gu and L. M. Zhu, "Motion control of piezoceramic actuators with creep, hysteresis and vibration compensation," *Sensors Actuators A: Phys.*, vol. 197, pp. 76–87, 2013.
[45] J. Sheng, H. Chen, B. Li, and L. Chang, "Temperature dependence of the dielectric constant of acrylic dielectric elastomer," *Appl. Phys. A*, vol. 110, no. 2, pp. 511–515, 2013.

Xingyu Chen (Student Member, IEEE) received the B.E. degree (with Hons.) in mechanical engineering from the Harbin Institute of Technology, Harbin, China, in 2023. He is currently working toward the M.S. degree in mechanical engineering with Shanghai Jiao Tong University, Shanghai, China.

His research interests include dynamic modeling and control of soft actuators.

Xiaotian Shi received the B.E. degree in mechanical engineering from Xi'an Jiaotong University, Xi'an, China, in 2022. He is currently working toward the Ph.D. degree in mechanical engineering, Shanghai Jiao Tong University, Shanghai, China.

His research interests include dielectric elastomer actuators and their applications in soft robotics and wearable haptic feedback.

Peinan Yan (Student Member, IEEE) received the B.E. degree in mechanical engineering in 2020 from Shanghai Jiao Tong University, Shanghai, China, where he is currently working toward the Ph.D. degree in mechanical engineering.

His research interests include design and control of dielectric elastomer actuators.

Jieji Ren received the B.E. degree in optical information science and technology and M.S. degree in optics from the Harbin Institute of Technology, Harbin, China, in 2013 and 2015, respectively, and the Ph.D. degree in mechanical engineering from Shanghai Jiao Tong University, Shanghai, China, in 2022.

He is currently a Postdoctoral Researcher with the Institute of Robotics, Shanghai Jiao Tong University. His research interests include vision-based tactile sensors, computer vision, and deep learning.

Guoying Gu (Senior Member, IEEE) received the B.E. degree (with Hons.) in electronic science and technology, in 2006, and the Ph.D. degree (with honors) in mechatronic engineering from Shanghai Jiao Tong University, Shanghai, China, in 2012.

He was a Humboldt Fellow with the University of Oldenburg, Oldenburg, Germany. He was a Visiting Scholar with the Massachusetts Institute of Technology, Cambridge, MA, USA, National University of Singapore, Singapore, and Concordia University, Montreal, QC, Canada. He is currently appointed as a Distinguished Professor with the School of Mechanical Engineering, Shanghai Jiao Tong University. He has authored or coauthored more than 150 publications, which have appeared in *Science, Science Robotics, Nature Biomedical Engineering, Nature Reviews Materials, Nature Materials, Nature Communications, Science Advances,* IEEE/ASME Transaction, *Advanced Materials, Soft Robotics, Science China* serials etc., as book chapters and in conference proceedings. His research interests include soft robotics, bioinspired and wearable robots, smart materials sensing, actuation, and motion control.

Dr. Gu was the recipient of the National Science Fund for Distinguished Young Scholars and the XPLORER Prize. He is currently an Associate Editor for *Soft Robotics* and was an Associate Editor for IEEE TRANSACTIONS ON ROBOTICS and IEEE ROBOTICS AND AUTOMATION LETTERS. He has also served for several journals as Editorial Board Member, Topic Editor, or Guest Editor, and several international conferences/symposiums as Chair, Co-Chair, Associate Editor, or Program Committee Member.

Jiang Zou (Member, IEEE) received the B.E. degree in mechanical engineering from the University of Science and Technology Beijing, Beijing, China, in 2014, and the Ph.D. degree in mechanical engineering from Shanghai Jiao Tong University, Shanghai, China, in 2019.

Since 2019, he has worked with Shanghai Jiao Tong University. He is currently an Associate Professor with the School of Mechanical Engineering. His research interests include design, modeling, and control of dielectric elastomer actuated soft robots. He has authored or coauthored more than 40 publications, which have appeared in *Science, Science Robotics, Nature Communications, National Science Review,* IEEE TRANSACTIONS ON ROBOTICS, etc.